nature physics

Article

https://doi.org/10.1038/s41567-024-02472-6

Multiphoton electron emission with non-classical light

Received: 25 July 2023

Accepted: 8 March 2024

Published online: 09 April 2024

Check for updates

Jonas Heimerl[1,4] ✉, Alexander Mikhaylov[2,4], Stefan Meier[1], Henrick Höllerer[1], Ido Kaminer[3], Maria Chekhova[1,2] & Peter Hommelhoff[1,2] ✉

Photon number distributions of classical and non-classical light sources have been studied extensively, yet their impact on photoemission processes is largely unexplored. In this article, we present measurements of electron number distributions from metal needle tips illuminated with ultrashort light pulses with various photon quantum statistics. By varying the photon statistics of the exciting light field between classical (Poissonian) and quantum (super-Poissonian), we demonstrate that the measured electron distributions are changed substantially. Using single-mode bright squeezed vacuum light, we measure extreme statistics events with up to 65 electrons from one light pulse at a mean of 0.27 electrons per pulse—the likelihood for such an event equals 10^{-128} with Poissonian statistics. By changing the number of modes of the exciting bright squeezed vacuum, we can tailor the electron number distribution on demand. Most importantly, our results demonstrate that the photon statistics is imprinted from the driving light to the emitted electrons, opening the door to new sensor devices and to strong-field optics with quantum light and electrons.

Strong optical fields facilitate high harmonic and attosecond pulse generation, the topic of the 2023 Nobel Prize in Physics. These phenomena rely on the thorough understanding of the photo-ionization and the rescattering of electrons[1–7]. Recently, these processes have been investigated theoretically, with the classical ultrafast laser field replaced by a strong quantum (that is, a non-classical) light field[8–14]. New scaling laws of the cut-off in high harmonic generation are obtained when going from classical to non-classical light fields[13].

Experimentally, non-classical light can be generated by parametric down-conversion (PDC) in nonlinear crystals. While weakly pumped PDC generates photon pairs, stronger pumping causes these pairs to overlap, forming a quantum state known as 'squeezed vacuum'. The electric field quadratures of squeezed vacuum have different quantum uncertainties, one of them below the vacuum level (squeezed), the other one anti-squeezed, according to the Heisenberg uncertainty relation (inset of Fig. 1b)[15,16]. The mean number of photons in squeezed vacuum is roughly given by the ratio of these uncertainties and can be very high, despite the term 'vacuum'. When strongly pumped, PDC generates squeezed vacuum so bright that it can even generate optical harmonics, hence it is called bright squeezed vacuum (BSV)[15,17]. Due to the presence of photon pairs, BSV light shows superbunched photon statistics. Pulsed BSV is characterized by intense interpulse and intrapulse photon number fluctuations, which lead to a very broad-tailed photon number distribution compared to coherent light, whose photon number distribution is Poissonian[17].

Such macroscopic quantum light states with extreme photon number events are inherently interesting to study, yet their interaction with matter becomes even more intriguing. In particular, do the extreme counting statistics prevail and are they even enhanced in nonlinear interactions? We here investigate how such highly fluctuating quantum light interacts with matter. With this light–matter interaction, we enter a new realm of strong-field physics, since this light cannot be described as a classical field any longer[13]. More specifically, we study nonlinear multiphoton photoemission from metal needle tips using pulsed BSV

[1]Department of Physics, Friedrich-Alexander-Universität Erlangen-Nürnberg (FAU), Erlangen, Germany. [2]Max Planck Institute for the Science of Light, Erlangen, Germany. [3]Department of Electrical and Computer Engineering, Russell Berrie Nanotechnology Institute, Technion-Israel Institute of Technology, Haifa, Israel. [4]These authors contributed equally: Jonas Heimerl, Alexander Mikhaylov. ✉e-mail: jonas.heimerl@fau.de; peter.hommelhoff@fau.de

https://doi.org/10.1038/s41567-024-02472-6

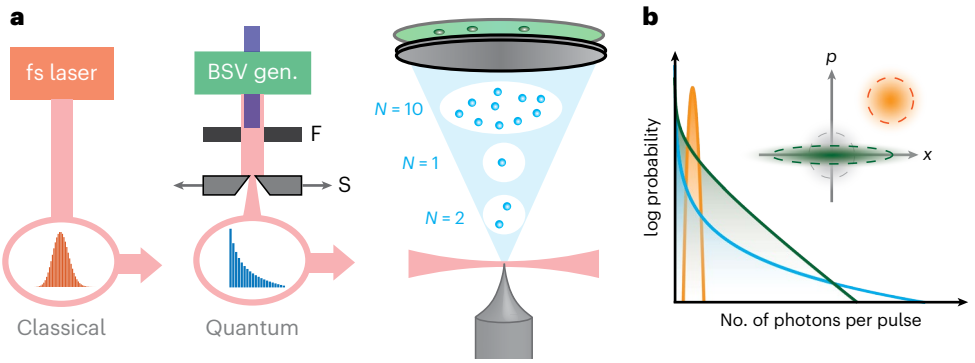

Fig. 1 | Experimental scheme. a, Sketch of the optical setup with the femtosecond erbium fibre laser system and BSV source based on PDC. To adjust the number of modes in BSV, spectral (F) and spatial filtering (S) is required, which we realize with variable bandpass filters and a variable slit (see text for details). Both pulsed beams are focused on the apex of a tungsten needle tip, in separate measurements. The emitted pulses of electrons (blue dots) are accelerated from the tip towards an MCP with a phosphor screen. We obtain the electron number distribution by counting the number of electrons N emitted for each light pulse. **b**, Schematic representations of photon number distributions for the coherent (orange) and the BSV light (green, first-order gamma distribution) with the same mean number of photons per pulse. We also show the fourth-order gamma distribution (blue), which exhibits an even heavier tail (see text for details). Inset: phase space diagrams of the quantum electric field for vacuum (grey), coherent light (orange) and squeezed vacuum (green), where x and p are amplitude and phase quadratures, respectively. The mean number of photons in squeezed vacuum is determined by the aspect ratio of the distribution, and it reaches up to 10^{10} for BSV. fs, femtosecond; gen., generation.

light, compared to pulsed coherent light that serves as the reference with Poissonian photon statistics.

The advantage of needle tips over atoms is that they typically require at least one order of magnitude smaller incident intensities to trigger electron emission, for two reasons: first, typically lower work function (ionization potentials) and second, the field enhancement effect happening at the tip apex, which concentrates the incident light field to the very tip, similar to the lightning rod effect[18–20].

We demonstrate that the electron number distribution resulting from BSV exhibits events even more extreme than the driving BSV itself: We observe extreme electron events that exceed the mean value by a factor of 240. This behaviour can be attributed to the interplay of BSV driving light and the nonlinearity of the emission process. We show that the photon number statistics of the exciting light are transferred to the emitted electron number distribution. Tailoring the number statistics of electron beams directly in the emission process is particularly intriguing for the field of imaging, especially electron-based imaging. We foresee that imprinting sub-Poissonian photon statistics[21] will enable sub-shot-noise imaging in the future, a highly important feature for interaction-lean imaging of biological samples[22–25].

In the experiment, we use two light sources: a pulsed laser beam emitting coherent light and a non-classical BSV source. The two sources are used alternatively as depicted in Fig. 1a. The coherent light source is a femtosecond erbium fibre laser with a central wavelength of 1,550 nm and a pulse duration of 170 fs. The BSV source is based on PDC in a 10 mm long type-I beta-barium borate crystal. The crystal is pumped with 800 nm laser light with a pulse duration of ~1.6 ps. The resulting BSV spectrum spans a broad range from 1,400 nm to 1,900 nm with a central wavelength of 1,600 nm. The pulse repetition rate for both sources is set to ~100 Hz by pulse picking.

The two light sources display vastly different photon number distributions. For coherent light, the photon number distribution is Poissonian[15] (Fig. 1(b)). In contrast, the photon statistics of BSV can be altered: when we gradually change the spatial and spectral filtering of the BSV, we go from multimode to the (nearly) single-mode case (Methods). This allows us to vary progressively its photon statistics. In the case of one spatial and spectral mode, the BSV photon statistics obeys a gamma distribution[17,26]

$$P_{\mathrm{BSV}}(N) = \frac{1}{\sqrt{2\pi\langle N\rangle N}} \mathrm{e}^{-\frac{N}{2\langle N\rangle}}, \qquad (1)$$

a broad distribution with the highest probability being zero photons per pulse always (Fig. 1b, green), where N is the number of photons and $\langle N\rangle$ the average number of photons per laser pulse. In the multimode case, the tail becomes smaller for an increasing number of modes[27].

To adjust the number of spectral modes in the BSV light beam, we use a bandpass filter with 50 nm full-width at half-maximum, with the central wavelength matching the degenerate wavelength of the BSV spectrum at 1,600 nm. We place a slit in the back Fourier plane of the lens, which collimates the BSV after the crystal (Fig. 1a). This slit allows us to filter the spatial modes. We ensure that the 800 nm pump light is well suppressed with a dichroic mirror and bandpass filters placed after the BSV generation optics.

Each beam can be sent to our vacuum chamber, where it is focused by an off-axis parabolic mirror onto a sharp tungsten needle tip with a typical apex radius of ~10 nm. The tip is situated in an ultra-high vacuum chamber with a base pressure of 1×10^{-9} hPa (Fig. 1a). The beam size for both beams is ~5 µm ($1/e^2$ intensity radius). This rather tight focusing allows us to reach peak intensities of ~5×10^{12} W cm^{-2} for the coherent case (Gaussian pulse) assuming a field enhancement of a factor of 6 at the tip apex[20]. The resulting intensity is sufficient to trigger notable electron emission via a nonlinear multiphoton process. For BSV, the available peak intensity depends on the filtering and the resulting ultrafast fluctuations. For unfiltered BSV, the intensity can reach up to 3×10^{12} W cm^{-2}, assuming a Gaussian envelope in time.

The emitted electrons are accelerated from the negatively biased tip (−200 V) towards a chevron-type microchannel plate detector (MCP) with a phosphor screen, serving as a spatially resolving single-electron detector: Each electron amplified by the MCP generates a bright spot on the phosphor screen, which is imaged with a charge-coupled device camera, whose frame acquisition is synchronized to the repetition rate of the excitation light pulses. To retrieve the electron number statistics, we determine the electron number N_e (number of bright spots) for each recorded frame, that is, for each light pulse, via an image recognition code. This way we register up to several hundred electrons per pulse. Typically, we record around $1–4 \times 10^4$ frames for each excitation power, corresponding to a few minutes of measurement time. We use these frames to determine the average number of detected electrons per pulse, μ. The MCP has a quantum efficiency of 50–85% (ref. 28) and shows a background of $\mu \approx 0.002$ counts per pulse, independent of the incoming electrons.

Figure 2 shows the results obtained with coherent light excitation. In Fig. 2a, the measured probability distribution of the number of

https://doi.org/10.1038/s41567-024-02472-6

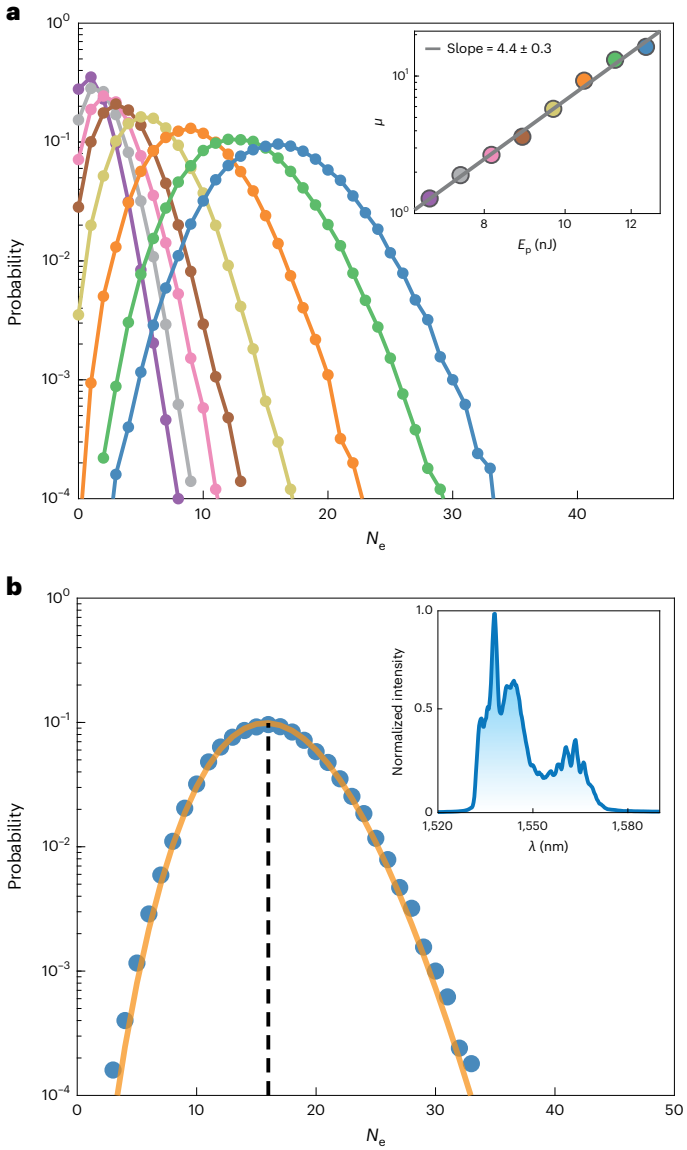

Fig. 2 | Electron number statistics with coherent excitation light. a, The electron number distributions, namely the detection probability plotted versus the number of detected electrons N_e, for various pulse energies. The maxima of the distributions shift towards higher mean values for increasing excitation light energy. The lines connecting the dots serve as a visual guide. The inset shows the double logarithmic plot of the mean number of the registered electrons per pulse μ versus the pulse energy E_p. The colour of each data point here matches the colour of the electron number distribution in the main graph. The slope of the curve obtained from fitting the inset data (solid grey line) indicates the nonlinearity of the photoemission process as $n = 4.4 \pm 0.3$. **b**, Example electron number distribution for a mean value of $\mu = 16.0$ and $E_p = 13$ nJ taken from **a**. The orange line shows the Poisson distribution calculated for $\mu = 16$. We observe almost perfect agreement between the analytical curve and the experiment, without any free parameter adjustment. Hence, the number statistics remains Poissonian, as expected. The inset shows the spectrum of the coherent light source, where the horizontal axis is the wavelength λ and the vertical axis is the normalized intensity.

detected electrons per pulse N_e is depicted. The probability is normalized to the total electron counts. The several curves of various colours correspond to different pulse energies E_p, spanning the range of 7–13 nJ. We observe that the maxima shift towards higher average values μ with increasing pulse energies, from $\mu = 1$ at $E_p = 7$ nJ to $\mu = 16$ at $E_p = 13$ nJ, as shown in the inset. Fitting these data yields a nonlinearity of $n = 4.4 \pm 0.3$ of the power scaling $\mu \propto (E_p)^n$, manifesting the four-photon excitation nature as the dominating contribution in the emission. The nonlinearity of this power scaling depends on the ratio of the work function of the material and the mean photon energy[29].

In Fig. 2b we pick the distribution with $\mu = 16.0$ ($E_p = 13$ nJ) and overlay an analytical Poisson distribution of the same mean (orange) for comparison. We note that the analytical curve matches the data almost perfectly, without any fitting. Such excellent agreement experimentally demonstrates that the multiphoton photoemission shows Poissonian electron number distributions, at well above one electron per pulse. Event-resolved electron number distributions have so far only been shown for single-photon photoemission or in conjunction with electron optics, influencing the number statistics, with well below one electron per laser pulse[30,31].

The Poissonian nature of the electron emission implies that each electron is emitted independently, even when there is clearly more than one electron per pulse emitted. In particular, we observe no hint of any blockade mechanism—even for large N_e—during the emission process, caused by either Coulomb interaction or Pauli exclusion, a surprising finding given the nanometre–femtosecond emission dimensions. Our findings suggest that achieving a Coulomb or Pauli blockade would necessitate an even higher degeneracy (electrons per phase space) at the emission process than the current one, which is on the order of $\sim 10^{-3}$ (refs. 32,33). Recently, Coulomb-induced two-electron energy correlations in free space after the emission have been shown to be rather strong in the energy domain, even for an average of less than one electron per laser pulse[30,31]. Resolving such energy anti-correlations is not possible in our case. However, we expect these correlations to be much weaker because of the ~14 times longer pulse duration compared to ref. 31.

We now use BSV light to trigger the photoemission. Figure 3a shows the obtained electron number distributions for various BSV pulse energies E_p in the range of 9–18 nJ, like above. Here, the BSV light is filtered spectrally with a 50 nm bandwidth filter at the degenerate wavelength, but so far, not spatially. We observe that events with higher electron numbers N_e (extreme events) become more likely as we increase the pulse energy, leading to broader distributions. Yet and notably, the highest probability remains at $N_e = 0$ for all pulse energies. The inset of Fig. 3a shows the nonlinear scaling of the mean values μ versus the excitation energies E_p. Fitting of this dependence yields a slope value of $n = 4.0 \pm 0.3$, similar to the coherent case.

Two parameters are crucial to understand the obtained BSV electron number distribution in detail, namely the nonlinearity n of the emission process and the number of optical modes m present at the tip apex. To accommodate the nonlinearity of an n-photon process pumped by a light with a gamma distribution equation (1) of photon numbers, a generalized nth-order gamma function is required (see ref. 17 for details):

$$P_n(N) = \frac{\sqrt[2n]{(2n-1)!!}}{n\sqrt{2\pi}\sqrt[2n]{\langle N\rangle}N^{1-1/2n}} e^{-\frac{1}{2}n\sqrt[n]{(2n-1)!!\frac{N}{\langle N\rangle}}}. \quad (2)$$

The overall shape of the generalized distributions is similar to the fundamental ($n = 1$) gamma distribution (Fig. 1b, but the tails become even heavier with increasing order n, for the same mean value, reflecting the nonlinear nature of the multiphoton emission process. Furthermore, BSV is of multimode nature in our case, which directly impacts the photon number distribution[27]: to obtain the theoretical m-th order multimode distribution, we have to convolve m single-mode probability distributions of the incident light because they are statistically independent (Methods).

The influence of both the nonlinearity and the number of modes on the obtained distributions is shown in Fig. 3b–d. We first investigate the case with many spatial modes and a narrow spectrum (Fig. 3b) for the highest BSV pulse energy of $E_p = 18$ nJ and an experimental

https://doi.org/10.1038/s41567-024-02472-6

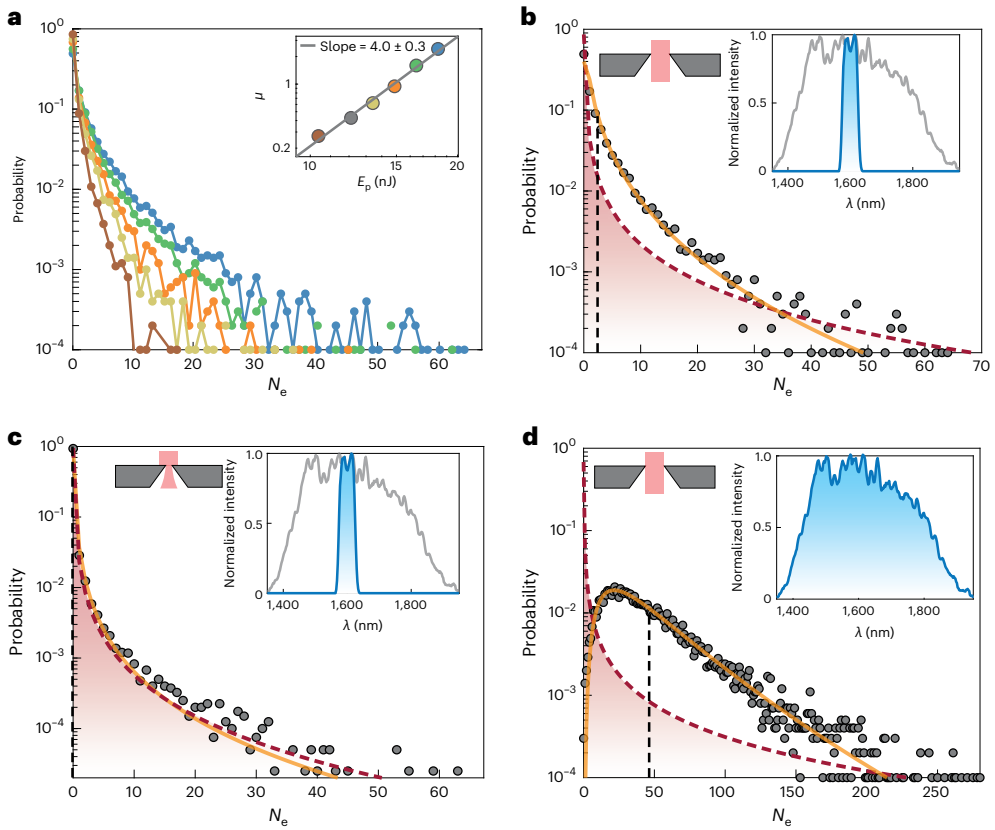

Fig. 3 | Electron number statistics with BSV as excitation light. a, Electron number distributions for various BSV pulse energies. Colours match the inset colours. Notably, all curves show the highest probability at $N_e = 0$. The BSV was filtered with a 50-nm-wide bandpass filter around the degenerate wavelength of 1,600 nm. The inset shows the nonlinear scaling of the mean number μ of emitted electrons per laser pulse versus the pulse energy E_p on a double logarithmic scale. The fit yields a slope of $n = 4.0 \pm 0.3$, similar to the coherent case. **b**–**d**, The effect of different spatial and spectral mode filtering on the electron number distribution, as indicated by the slit size (upper left insets) and by the spectral filtering (upper right insets). The analytical curves (dashed red) always depict the single-mode case ($m = 1$) for a fourth-order nonlinearity ($n = 4$), that is, they show a fourth-order gamma distribution for the measured mean value (black dashed line). **b**, Electron number distribution with experimental mean value $\mu = 2.6$ from **a** for the highest pulse energy of $E_p = 18$ nJ, showing the best agreement for $m = 11 \pm 3$ modes (orange). **c**, With spatially and spectrally filtered BSV together with the theoretical curves for $m = 1$ (red) and $m = 2$ (orange). Extreme events of up to 65 electrons per pulse are observed, several orders of magnitude higher than the mean value $\mu = 0.27$, demonstrating the extreme fluctuations of BSV imprinted on the photo-emitted electrons. **d**, Using completely unfiltered BSV, mean values as high as $\mu = 48$ can be observed. Due to uncompensated group velocity dispersion in the optics beam path, the number of modes increases to $m = 57 \pm 5$ (see text for details). In stark contrast to the single-mode case, the distribution maximum is now clearly shifted away from 0.

mean value of $\mu = 2.6$. We compute the generalized gamma functions with the nonlinearity of $n = 4$ fixed and vary the number of modes m to infer which m values reproduce the experimental curves the best. We find the best agreement for $m = 11 \pm 3$ (orange), clearly deviating from the single-mode distribution (red). We note that the quantum efficiency of the MCP lowers the mean number of detected electrons but does not change the shape of the distribution, similar to the optics case[34].

Now we close the slit down to a few hundred micrometres, which reduces the number of spatial modes but also the available pulse energy ($E_p = 6$ nJ maximum), see Fig. 3c. Here we also plot the analytical distributions for $m = 1$ (red) and $m = 2$ (orange), still with $n = 4$. Clearly, the experimental distribution is now very close to the single-mode fourth-order gamma distribution. Notably, we observe large electron number fluctuations reaching up to extreme events of 65 electrons per pulse, despite the small mean value of $\mu = 0.27$. We note that the probability of detecting such an event with a Poissonian distribution with a mean of 0.27 would be 10^{-128}. The probability of detecting the same number of electrons per pulse for the same mean value in the linear case ($n = 1$), that is single-photon emission, is 48 orders of magnitudes lower[17]. This factor demonstrates that the fluctuations are becoming highly amplified by the nonlinear emission process.

The number of time-frequency modes is given by the ratio between the detector resolution and the coherence time of the light, in our case the coherence time of the BSV[15,35]. Therefore, a single-mode distribution can only be observed if the response time of the detector—in the case here, the tip—is smaller than the coherence time of the light. The fact that we observe the single-mode gamma distribution for the electrons indicates that the electron emission follows the ultrafast fluctuations present in broadband BSV. This behaviour results from the emission process, which is prompt on the (sub-) femtosecond time scale[36–38], which is small compared to the coherence time of ~170 fs of BSV, corresponding to the spectral bandwidth of 50 nm. We note that, similar to averaging over many pulses, different temporal emission events within one pulse do not lead to multiple modes as long as intensity fluctuations of the light are not washed out. Clearly, such a (sub-) femtosecond response time is out of reach for even the fastest photodiodes. For comparison, such a photodiode could only detect the averaged photon number distribution of roughly ~20 temporal modes present for the given bandwidth[34].

Interestingly, already small admixtures of a few percent Poissonian-governed emission would change the single-mode electron number distribution and shift the maximum of the distribution to larger N_e values (Methods). While field-emitted electrons show

Poissonian emission statistics[39], our measurements indicate that the quantum statistics of the light field alone determines the electron number distribution for (multiphoton) photoemission, similar to optical harmonics generated from BSV light[17].

To contrast the single-mode scenario, we show in Fig. 3d the electron number distribution obtained with neither spatially nor spectrally filtered broadband BSV light. Overall, the higher pulse energy of $E_p = 36$ nJ in this case allows us to reach a higher mean value of $\mu = 48$ and up to 300 electrons per pulse. The highest probability of detecting electrons is clearly shifted now to $N_e = 22$. For this unfiltered configuration, we find the best agreement between experimental and multimode gamma distribution for $m = 57 \pm 5$ (orange curve).

Clearly, the extreme events compared to the mean value are heavily reduced here as the distribution gradually evolves into a Poisson distribution. This decrease in fluctuations can be explained by the increase in the number of temporal modes: The increased bandwidth reduces the coherence time down to ~14 fs, which is still much larger than the emission time of the electrons. Yet, the spectrum of such spectrally broadband BSV light (inset in Fig. 3d) adds another degree of complexity. In this case, group delay dispersion cannot be neglected anymore. Due to optical elements along the optics beam path, a group delay dispersion of roughly -400 ± 100 fs^2 at the central wavelength accumulates. For a coherent Fourier-limited laser pulse with the same bandwidth, the initial pulse duration (13 fs) would broaden by a factor of ~5–6, which would not change the Poissonian electron number distribution. For the BSV case, however, different temporal modes disperse and mix at the tip apex. In other words, initially correlated photon pairs no longer arrive at the same time anymore. Hence, the tip, being a prompt detector with a sub-femtosecond response time as shown above, tells these events apart, which is why they do not lead to a spike in the multiphoton emission as they would if the photons arrived simultaneously, that is, within the tip's response time. As an effect, the tip detector averages over these dispersed modes[40], which explains the increase in modes from $m = 11$ (Fig. 3b) to $m = 57$ (Fig. 3d). The ratio of these mode numbers, roughly equalling 5, is of similar size to the temporal broadening we would expect for coherent light pulses, governed by dispersive effects.

In summary, our results show we can imprint various photon number distributions on photo-emitted electrons. With coherent femtosecond laser pulses, we observe clean Poissonian electron number statistics. With non-classical BSV light, we can vary the counting statistics of emitted electrons by adjusting the number of spatial and temporal modes of the BSV present at the tip apex. Most importantly, we have shown that the emitted electrons inherit the photon number statistics of the driving light. We expect this to hold not only for super-Poissonian light statistics like shown here but also for sub-Poissonian light statistics, which may have direct implications for electron imaging applications: Both in light and electron optics, the imaging quality improves if the statistics becomes sub-Poissonian, that is, the variance of the number of photons or electrons becomes smaller than their mean value[25,41]. Beating the shot-noise limit in this way, such a scheme to generate sub-Poissonian electron beams might find direct applications in advanced electron microscopy. Bright sub-Poissonian light sources like high-number Fock states to trigger nonlinear electron emission are not available yet. However, proper light sources for the linear photoemission regime are available through applying the heralding technique to twin-beam BSV[21].

We have generated non-classical electron statistics through the electron emission process, rather than via filtering[30,31,42], which almost always comes at the cost of losing brightness. More generally, our work paves the way to tailor-make photon distributions and transfer them into the electron realm (and vice versa[43]), not only to venture deeper into quantum electron optics but also for various applications beyond sub-shot-noise imaging[44]. Finally, the intensities present in our experiment are large enough to drive electrons strongly in the light field, opening the door to the nascent research field of strong-field electron quantum optics[45].

Online content

Any methods, additional references, Nature Portfolio reporting summaries, source data, extended data, supplementary information, acknowledgements, peer review information; details of author contributions and competing interests; and statements of data and code availability are available at https://doi.org/10.1038/s41567-024-02472-6.

References

1. L'Huillier, A., Lompre, L. A., Mainfray, G. & Manus, C. Multiply charged ions formed by multiphoton absorption processes in the continuum. *Phys. Rev. Lett.* **48**, 1814–1817 (1982).
2. Ferray, M. et al. Multiple-harmonic conversion of 1064 nm radiation in rare gases. *J. Phys. B At. Mol. Opt. Phys.* **21**, 31–35 (1988).
3. Corkum, P. B. Plasma perspective on strong field multiphoton ionization. *Phys. Rev. Lett.* **71**, 1994–1997 (1993).
4. Lewenstein, M., Balcou, P., Ivanov, M. Y., L'Huillier, A. & Corkum, P. B. Theory of high-harmonic generation by low-frequency laser fields. *Phys. Rev. A* **49**, 2117–2132 (1994).
5. Baltuška, A. et al. Attosecond control of electronic processes by intense light fields. *Nature* **421**, 611–615 (2003).
6. Schultze, M. et al. Delay in photoemission. *Science* **328**, 1658–1662 (2010).
7. Krausz, F. & Stockman, M. I. Attosecond metrology: from electron capture to future signal processing. *Nat. Photonics* **8**, 205–213 (2014).
8. Tsatrafyllis, N., Kominis, I.K., Gonoskov, I.A. & Tzallas, P. High-order harmonics measured by the photon statistics of the infrared driving-field exiting the atomic medium. *Nat. Commun.* **8**, 15170 (2017); https://doi.org/10.1038/ncomms15170
9. Tsatrafyllis, N. et al. Quantum optical signatures in a strong laser pulse after interaction with semiconductors. *Phys. Rev. Lett.* **122**, 193602 (2019); https://doi.org/10.1103/physrevlett.122.193602
10. Lewenstein, M. et al. Generation of optical Schrödinger cat states in intense laser-matter interactions. *Nat. Phys.* **17**, 1104–1108 (2021).
11. Gorlach, A., Neufeld, O., Rivera, N., Cohen, O. & Kaminer, I. The quantum-optical nature of high harmonic generation. *Nat. Commun.* **11**, 4598 (2020); https://doi.org/10.1038/s41467-020-18218-w
12. Stammer, P. et al. Quantum electrodynamics of intense laser-matter interactions: a tool for quantum state engineering. *PRX Quantum* **4**, 010201 (2023); https://doi.org/10.1103/prxquantum.4.010201
13. Gorlach, A. et al. High-harmonic generation driven by quantum light. *Nat. Phys.* **19**, 1689–1696 (2023).
14. Even Tzur, M. & Cohen, O. Motion of charged particles in bright squeezed vacuum. *Light Sci. Appl.* **13**, 41 (2023).
15. Mandel, L. & Wolf, E. *Optical Coherence and Quantum Optics* (Cambridge Univ. Press, 1995).
16. Andersen, U. L., Gehring, T., Marquardt, C. & Leuchs, G. 30 years of squeezed light generation. *Phys. Scr.* **91**, 053001 (2016).
17. Manceau, M., Spasibko, K.Y., Leuchs, G., Filip, R. & Chekhova, M.V. Indefinite-mean pareto photon distribution from amplified quantum noise. *Phys. Rev. Lett.* **123**, 123606 (2019); https://doi.org/10.1103/physrevlett.123.123606
18. Weber, T. et al. Correlated electron emission in multiphoton double ionization. *Nature* **405**, 658–661 (2000).
19. Novotny, L. & Hecht, B. *Principles of Nano-optics* (Cambridge Univ. Press, 2012).
20. Thomas, S., Krüger, M., Förster, M., Schenk, M. & Hommelhoff, P. Probing of optical near-fields by electron rescattering on the 1 nm scale. *Nano Lett.* **13**, 4790–4794 (2013).

21. Iskhakov, T. S. et al. Heralded source of bright multi-mode mesoscopic sub-Poissonian light. *Opt. Lett.* **41**, 2149–2152 (2016).
22. Henderson, R. The potential and limitations of neutrons, electrons and x-rays for atomic resolution microscopy of unstained biological molecules. *Q. Rev. Biophys.* **28**, 171–193 (1995).
23. Okamoto, H. Possible use of a Cooper-pair box for low-dose electron microscopy. *Phys. Rev. A* **85**, 043810 (2012); https://doi.org/10.1103/physreva.85.043810
24. Kruit, P. et al. Designs for a quantum electron microscope. *Ultramicroscopy* **164**, 31–45 (2016).
25. Berchera, I. R. & Degiovanni, I. P. Quantum imaging with sub-Poissonian light: challenges and perspectives in optical metrology. *Metrologia* **56**, 024001 (2019).
26. Leuchs, G., Glauber, R. J. & Schleich, W. P. Dimension of quantum phase space measured by photon correlations. *Phys. Scr.* **90**, 074066 (2015).
27. Allevi, A. & Bondani, M. Direct detection of super-thermal photon-number statistics in second-harmonic generation. *Opt. Lett.* **40**, 3089 (2015).
28. Wiza, J. L. et al. Microchannel plate detectors. *Nucl. Instrum. Methods* **162**, 587–601 (1979).
29. Krüger, M., Lemell, C., Wachter, G., Burgdörfer, J. & Hommelhoff, P. Attosecond physics phenomena at nanometric tips. *J. Phys. B At. Mol. Opt. Phys.* **51**, 172001 (2018).
30. Haindl, R. et al. Coulomb-correlated electron number states in a transmission electron microscope beam. *Nat. Phys.* **19**, 1410–1417 (2023).
31. Meier, S., Heimerl, J. & Hommelhoff, P. Few-electron correlations after ultrafast photoemission from nanometric needle tips. *Nat. Phys.* **19**, 1402–1409 (2023).
32. Silverman, M. On the feasibility of observing electron antibunching in a field-emission beam. *Phys. Lett. A* **120**, 442–446 (1987).
33. Lougovski, P. & Batelaan, H. Quantum description and properties of electrons emitted from pulsed nanotip electron sources. *Phys. Rev. A* **84**, 023417 (2011).
34. Spasibko, K. Y. et al. Multiphoton effects enhanced due to ultrafast photon-number fluctuations. *Phys. Rev. Lett.* **119**, 223603 (2017); https://doi.org/10.1103/physrevlett.119.223603
35. Ivanova, O. A., Iskhakov, T. S., Penin, A. N. & Chekhova, M. V. Multiphoton correlations in parametric down-conversion and their measurement in the pulsed regime. *Quantum Electron.* **36**, 951–956 (2006).
36. Hommelhoff, P., Kealhofer, C. & Kasevich, M.A. Ultrafast electron pulses from a tungsten tip triggered by low-power femtosecond laser pulses. *Phys. Rev. Lett.* **97**, 247402 (2006); https://doi.org/10.1103/physrevlett.97.247402
37. Piglosiewicz, B. et al. Carrier-envelope phase effects on the strong-field photoemission of electrons from metallic nanostructures. *Nat. Photon.* **8**, 37–42 (2013).
38. Dienstbier, P. et al. Tracing attosecond electron emission from a nanometric metal tip. *Nature* **616**, 702–706 (2023).
39. Kiesel, H., Renz, A. & Hasselbach, F. Observation of Hanbury Brown–Twiss anticorrelations for free electrons. *Nature* **418**, 392–394 (2002).
40. Kopylov, D. A., Rasputnyi, A. V., Murzina, T. V. & Chekhova, M. V. Spectral properties of second, third and fourth harmonics generation from broadband multimode bright squeezed vacuum. *Laser Phys. Lett.* **17**, 075401 (2020).
41. Gover, A., Nause, A., Dyunin, E. & Fedurin, M. Beating the shot-noise limit. *Nat. Phys.* **8**, 877–880 (2012).
42. Keramati, S., Brunner, W., Gay, T. J. & Batelaan, H. Non-Poissonian ultrashort nanoscale electron pulses. *Phys. Rev. Lett.* **127**, 180602 (2021); https://doi.org/10.1103/physrevlett.127.180602
43. Pizzi, A., Gorlach, A., Rivera, N., Nunnenkamp, A. & Kaminer, I. Light emission from strongly driven many-body systems. *Nat. Phys.* **19**, 551–561 (2023).
44. Marín-Suárez, M., Peltonen, J. T., Golubev, D. S. & Pekola, J. P. An electron turnstile for frequency-to-power conversion. *Nat. Nanotechnol.* **17**, 239–243 (2022).
45. Tzur, M. E. et al. Photon-statistics force in ultrafast electron dynamics. *Nat. Photon.* **17**, 501–509 (2023).

Methods

BSV generation

We here give more details on the generation of BSV. To generate BSV, we focus the pump beam (pulse duration 1.6 ps, energy per pulse up to 0.4 mJ) with a 700 mm cylindrical lens into a 10 mm beta-barium borate crystal cut for collinear degenerate type-I phase matching. The beam remains broad (~3 mm) in the optic axis plane, which eliminates the spatial walk-off effect[46]. The orientation of the crystal is set for a nearly collinear degenerate regime. We note that in the same configuration, various other unwanted accompanying processes inside the same crystal—such as saturable absorption, second-harmonic and sum-frequency generation—could be observed[47]. Such effects might result in an uncontrolled change of BSV photon statistics or even the intensity reduction. To alleviate the impact of these processes, we slightly detune the crystal from its optimal PDC phase-matching angle, reducing purposely the BSV intensity and keeping the maximum average pump power below 2 W. The pump laser power is kept fixed in all the measurements. To suppress the pump beam after the crystal, we use a dichroic mirror and bandpass filters with a total optical density of 22 at 800 nm.

In general, BSV has many spatial modes. All spatial modes present at the tip apex contribute to the emission process. Hence, to observe single-mode statistics in the electrons, the BSV has to be filtered before we send it to the tip. To filter a single spatial mode, we place a slit in the Fourier plane of a lens, which reduces the number of spatial modes. Therefore, the width of the slit sets the number of modes present at the tip apex.

The influence of an additional electron emission process on electron number statistics

As we have shown in the main text, we were able to imprint the statistics of BSV onto the electron number distribution. The measured fourth-order single-mode distribution of the number of electrons indicates that the electron emission is only driven by the light field, which we show in the following. In Extended Data Fig. 1a we show the theoretical single-mode fourth-order gamma distribution (equation (2)) of electrons with a mean value $\mu = 1$. We now assume that there is an additional emission process which does not depend on the driving light field. For this contribution, we choose a Poissonian electron number distribution, which is obtained in the d.c. field emission case, for example, in the absence of light. Because the two contributions are independent, the resulting electron number probability distribution will be given by the convolution of both distributions, shown by the yellow curve in Extended Data Fig. 1b–d. For a 1% admixture of Poissonian contribution (Extended Data Fig. 1b), only small differences to the original distribution are observed. Deviations from the single-mode case start already at 10% admixture, visible for electron events up to $N_e = 3$. For 50% admixture, the resulting distribution clearly deviates from the single-mode case.

Furthermore, the single-mode distribution in the experiment indicates that the electron bath at the tip apex acts collectively (coherently). If the tip apex acted as k independent emitters, we would get the incoherent sum of these k emission sites, being again the k-times convolution of the single-mode distribution.

Effect of multiple modes

As shown in the main text, the number of modes present at the tip apex crucially determines the electron number distribution. In the generalized gamma distribution, equation (2), the nonlinear scaling power and the mean number of electrons per light pulse are the only free parameters. However, when m independent modes are present at the tip apex, the resulting probability distribution is a convolution of m single-mode distributions. For the linear case of $n = 1$, the analytic formula is

$$P(N,m) = \frac{N^{m/2-1}}{\Gamma(m/2)}\left(\frac{m}{2\langle N\rangle}\right)^{m/2} \mathrm{e}^{-\frac{mN}{2\langle N\rangle}}, \tag{3}$$

where m is the number of modes, and $\Gamma(x)$ is the gamma function[15,27,47]. Extended Data Fig. 2a shows the distribution of equation (3) calculated for different numbers of modes m, the mean number of electrons being $\mu_e = 48$ in all cases. We observe that the distribution shifts from the left- to the right-hand side, approaching the Poissonian case (blue dashed line).

In the case of electron emission with nonlinearity n (ref. 17), this distribution becomes

$$P(N,m) = \frac{1}{n\Gamma(m/2)}\left(\frac{m}{2}\right)^{m/2} N^{\frac{m-2n}{2n}}\left(\langle N\rangle^{(1/n)}((2n-1)!!)^{-1/n}\right)^{-m/2} \times \exp\left(-\frac{mN^{1/n}((2n-1)!!)^{1/n}}{2\langle N\rangle^{1/n}}\right), \tag{4}$$

where the mean $\langle N\rangle$ must be chosen such that the condition

$$\sum_{N_0}^{N_{\max}} P(N,m)N = \mu_{\exp} \tag{5}$$

is fulfilled with $\mu_{\exp}$ being the experimental mean. In Fig. 2b, we show the distributions for $n = 4$ for different numbers of modes and the same mean number of electrons $\mu_e = 48$.

We note that equations (3) and (4) both diverge for $N = 0$ if $m = 1$. This is a mathematical consequence of fitting a discrete-variable distribution with a continuous-variable one, necessary to account for nonlinear emission processes, as shown already in the optics case[17].

Data availability

Source data are provided with this paper. All other data that support the plots within this paper and other findings of this study are available from the corresponding author upon reasonable request.

References

46. Chekhova, M. & Banzer, P. *Polarization of Light: In Classical, Quantum, and Nonlinear Optics* (De Gruyter, 2021); https://doi.org/10.1515/9783110668025
47. Spasibko, K. Spectral and statistical properties of high-gain parametric down-conversion. Preprint at https://doi.org/10.48550/arXiv.2007.12999 (2020).

Acknowledgements

This research was supported by the European Research Council (Consolidator Grant NearFieldAtto and Advanced Grant AccelOnChip) and the Deutsche Forschungsgemeinschaft (DFG, German Research Foundation) under Project ID 429529648–TRR 306 QuCoLiMa ('Quantum Cooperativity of Light and Matter') and Sonderforschungsbereich 953 ('Synthetic Carbon Allotropes'), Project ID 182849149. Furthermore, this research was supported by the Gordon and Betty Moore Foundation, Grant ID 11473. J.H. acknowledges funding from the Max Planck School of Photonics.

Author contributions

J.H. and A.M. measured the electron number distributions with non-classical light. J.H., S.M. and H.H. measured the distributions with the coherent light source. J.H. and A.M. analysed the data and generated the plots. I.K., M.C. and P.H. conceived the experiment. All authors contributed to writing the manuscript.

Competing interests

The authors declare no competing interests

Additional information

Extended data is available for this paper at https://doi.org/10.1038/s41567-024-02472-6.

Supplementary information The online version contains supplementary material available at https://doi.org/10.1038/s41567-024-02472-6.

Correspondence and requests for materials should be addressed to Jonas Heimerl or Peter Hommelhoff.

Peer review information *Nature Physics* thanks Peter Baum and the other, anonymous, reviewer(s) for their contribution to the peer review of this work.

https://doi.org/10.1038/s41567-024-02472-6

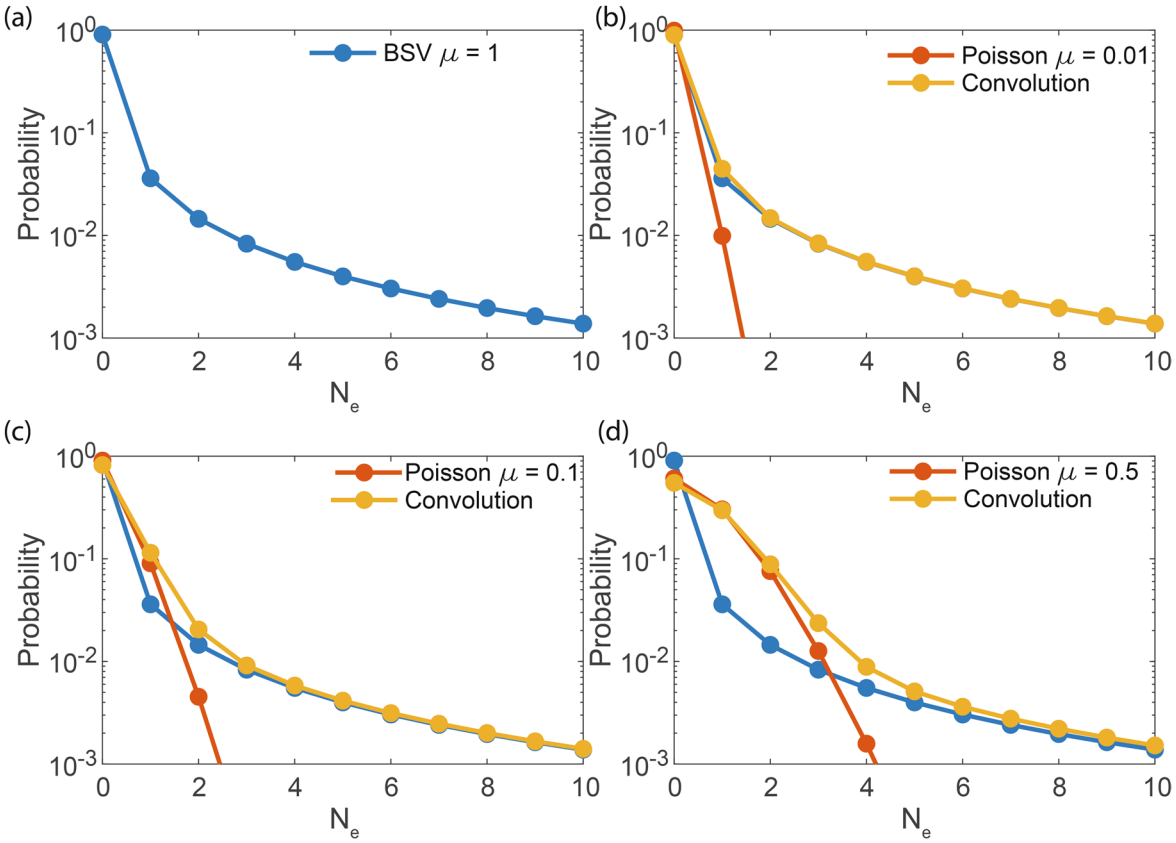

Extended Data Fig. 1 | The influence of an additional electron emission process on electron-number statistics. (a) Electron-number distribution for single-mode fourth-order Gamma distribution (blue) for an average of $\mu = 1$ electrons per laser pulse, calculated from Eq. (2) (see main text). Lines are guide to the eye. (b)-(d) Blue are the distributions from (a). Orange are Poisson distributions corresponding to mean numbers of electrons (b) $\mu = 0.01$, (c) $\mu = 0.1$ and (d) $\mu = 0.5$. The yellow curves are the corresponding convolutions of the Gamma distribution and the Poisson distribution. For increasing Poissonian admixture we observe a clear deviation from the original distribution in (a).

https://doi.org/10.1038/s41567-024-02472-6

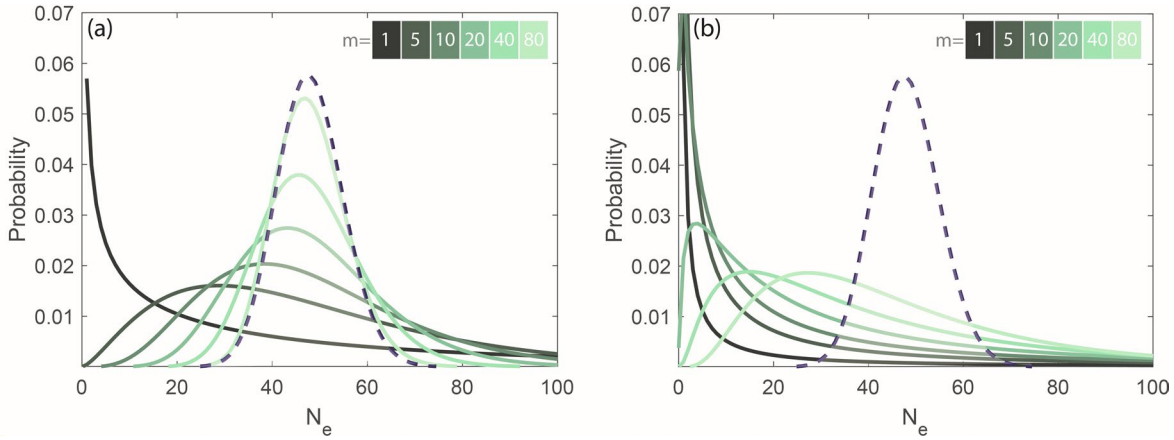

Extended Data Fig. 2 | The influence of the number of modes. Influence of number of modes $m = 1, 5, 20, 40, 80$ on the generalized Gamma distribution for (a) linear case ($n = 1$) and (b) the non-linear case ($n = 4$). for the same mean value of $\mu_e = 48$. The blue dashed line represents the Poissonian case in both cases.